CEAS-GNC-2024-008

EuroGNC Navigation Guidance Control CEAS Bristol, UK June 11th-13th 2024
University of BRISTOL ROYAL AERONAUTICAL SOCIETY AIAA

Linear Parameter-Varying gain-scheduled attitude controller for a spinning spacecraft involving large flexible booms

Ricardo Rodrigues Ph.D. student, Fédération de recherche ONERA - ENAC - ISAE SUPAERO, Université de Toulouse, 31055, Toulouse, France. ricardo.rodrigues@isae-supaero.fr

Francesco Sanfedino Associate Professor, Fédération de recherche ONERA - ENAC - ISAE SUPAERO, Université de Toulouse, 31055, Toulouse, France. francesco.sanfedino@isae-supaero.fr

Daniel Alazard Professor, Fédération de recherche ONERA - ENAC - ISAE SUPAERO, Université de Toulouse, 31055, Toulouse, France. daniel.alazard@isae-supaero.fr

ABSTRACT

In this paper, a comprehensive methodology is presented for modeling a spinning flexible spacecraft mission scenario and designing a gain-scheduled feedback control system that can robustly meet performance requirements and adapt to the angular velocity of the spacecraft. This spacecraft is composed of a main central body, two flexible booms and two tip masses. The model of the satellite was designed to be compliant with the Two-Input-Two-Output Port (TITOP) approach, which offers the possibility to model complex multibody mechanical systems, while keeping the uncertain nature of the plant and condensing all the possible mechanical configurations in a single linear fractional representation (LFR). Furthermore, the model fully captures the impact of centrifugal stiffening and softening on the dynamics of the satellite's flexible rotating booms, as well as its dependence on the angular velocity. Ultimately, the control design considers the interactions between subsystems and uncertainties, as well as the time-varying and coupled flexible dynamics.

Keywords: Robust $\mathcal{H}_\infty$ Control; Flexible Structures; LFT Modeling; Spinning Satellites; Multibody Dynamics

Nomenclature

$\mathbf{a}_P^{\mathcal{B}} \equiv \left.\frac{d\mathbf{v}_P^{\mathcal{B}}}{dt}\right|_{\mathcal{R}_i}$ = Inertial linear acceleration vector of the body $\mathcal{B}$ at the point P, expressed in $\mathrm{m\,s^{-2}}$.

$\dot{\mathbf{v}}_P^{\mathcal{B}} \equiv \left.\frac{d\mathbf{v}_P^{\mathcal{B}}}{dt}\right|_{\mathcal{R}_b}$ = Linear acceleration vector of the body $\mathcal{B}$ computed at the point P with respect to the body frame $\mathcal{R}_b$, expressed in $\mathrm{m\,s^{-2}}$.

$\dot{\boldsymbol{\omega}}_P^{\mathcal{B}}$ = Inertial angular acceleration vector of the body $\mathcal{B}$ at the point P, expressed in $\mathrm{rad\,s^{-2}}$.

$\mathbf{v}_P^{\mathcal{B}} \equiv \left.\frac{d\mathbf{x}_P}{dt}\right|_{\mathcal{R}_i}$ = Inertial velocity vector of the body $\mathcal{B}$ at the point P, expressed in $\mathrm{m\,s^{-1}}$.

$\boldsymbol{\omega}_P^{\mathcal{B}}$ = Inertial angular velocity vector of the body $\mathcal{B}$ at the point P, expressed in $\mathrm{rad\,s^{-1}}$.

$\mathbf{x}_P^{\mathcal{B}}$ = Distance vector defined between the point O, the origin of the inertial frame,
= and the point P of the body $\mathcal{B}$, expressed in m.
$\mathbf{BP}$ = Distance vector defined between the points B and P, expressed in m.
$\mathbf{\Theta}_P^{\mathcal{B}}$ = Euler angles vector of the body $\mathcal{B}$ computed at the point P with respect
= to the inertial frame, expressed in rad and using the 'ZYX' sequence of rotations.
$\mathbf{F}_{\text{ext}/\mathcal{B},G}$ = External forces vector applied to the body $\mathcal{B}$ at the point G, expressed in N.
$\mathbf{T}_{\text{ext}/\mathcal{B},G}$ = External torques vector applied to the body $\mathcal{B}$ at the point G, expressed in N m.
$\mathbf{F}_{\mathcal{B}/\mathcal{A},G}$ = Forces vector applied by the body $\mathcal{B}$ to the body $\mathcal{A}$ at the point G, expressed in N.
$\mathbf{T}_{\mathcal{B}/\mathcal{A},G}$ = Torques vector applied by the body $\mathcal{B}$ to the body $\mathcal{A}$ at the point G, expressed
= in N m.
$\mathbf{W}_{\mathcal{B}/\mathcal{A},G}$ = Wrench vector applied by the body $\mathcal{B}$ to the body $\mathcal{A}$ at the point G:
= $\mathbf{W}_{\mathcal{B}/\mathcal{A},G} = \left[\mathbf{F}_{\mathcal{B}/\mathcal{A},G}^{\mathrm{T}}, \mathbf{T}_{\mathcal{B}/\mathcal{A},G}^{\mathrm{T}}\right]^{\mathrm{T}}$, expressed in $[\mathrm{N}, \mathrm{N\,m}]$.
$[\mathbf{X}]_{\mathcal{R}_\bullet}$ = $\mathbf{X}$ (model, vector or tensor) expressed in the frame $\mathcal{R}_\bullet$.
$\mathbf{X}$ = $\mathbf{X}$ (model, vector or tensor) expressed in the body frame, unless stated otherwise.
$\mathbf{m}_P^{\mathcal{B}}$ = Motion vector of the body $\mathcal{B}$ at the point P:
= $\mathbf{m}_P^{\mathcal{B}} = \left[\dot{\mathbf{v}}_P^{\mathcal{B}^{\mathrm{T}}}, \dot{\boldsymbol{\omega}}_P^{\mathcal{B}^{\mathrm{T}}}, \mathbf{v}_P^{\mathcal{B}^{\mathrm{T}}}, \boldsymbol{\omega}_P^{\mathcal{B}^{\mathrm{T}}}, \mathbf{x}_P^{\mathcal{B}^{\mathrm{T}}}, \mathbf{\Theta}_P^{\mathcal{B}^{\mathrm{T}}}\right]^{\mathrm{T}}$.
$\mathbf{P}_{\mathcal{R}_a/\mathcal{R}_b}$ = DCM from the frame $\mathcal{R}_a$ to the frame $\mathcal{R}_b$ ($[\mathbf{v}]_{\mathcal{R}_b} = \mathbf{P}_{\mathcal{R}_a/\mathcal{R}_b}\,[\mathbf{v}]_{\mathcal{R}_a}$ for any vector $\mathbf{v}$).
$\mathbf{v}\{i\}$ = Component i of vector $\mathbf{v}$.
$\|\mathbf{v}\|_2$ = Euclidean norm of the vector $\mathbf{v}$.
$\hat{\mathbf{v}} = \dfrac{\mathbf{v}}{\|\mathbf{v}\|_2}$ = Normalized vector $\hat{\mathbf{v}}$ of a non-zero vector $\mathbf{v}$ (or unit vector in the direction of $\mathbf{v}$).
$\dot{\mathbf{x}}(t)$ = First time derivative of $\mathbf{x}$ with respect to the body frame.
$\mathbf{X}_{(\mathbf{I},\mathbf{J})}$ = Subsystem of $\mathbf{X}$ from the inputs indexed in the vector $\mathbf{J}$ to the outputs indexed
= in the vector $\mathbf{I}$ (if $(\mathbf{I},\mathbf{J}) = (:, 7:10)$, it means that one is considering the subsystem
= between the inputs from 7 until 10 to all the outputs).
$\mathrm{diag}(\mathbf{A}, \cdots)$ = Block-diagonal augmented matrix.
$\overline{\mathbf{x}}$ = Equilibrium value of $\mathbf{x}$.
$\delta\mathbf{x}$ = Small variation of $\mathbf{x}$ around a defined equilibrium.
$\mathbf{I}_n$ = Identity matrix $n \times n$.
$\mathbf{0}_{n\times m}$ = Zero matrix $n \times m$.
$\mathbf{J}_G^{\mathcal{B}}$ = Inertia tensor of $\mathcal{B}$, computed at the point G, written in $\mathcal{R}_b$ and expressed in kg m^2.
$m^{\mathcal{B}}$ = Mass of $\mathcal{B}$ expressed in kg.
s = Laplace's variable.

1 Introduction

The study of flexural vibration modes in rotating beams has driven extensive research in the design of helicopter rotor systems, wind turbines and various other devices [1]. The application of structures modeled as rotating beams is also very common in spacecraft applications, where long, flexible and rotating space booms [2] or high-gain antennas are frequently employed, as seen in missions like Cluster [3] or the proposed Turbulence Heating ObserveR (THOR) satellite [4]. Consequently, there is extensive literature dedicated to exploring the dynamics and vibrations of these structures [5]. Traditionally, these components were designed using rigid materials. However, the current trend is to employ more flexible and lightweight structures. This trend is particularly significant in space missions.

From the perspective of the Attitude and Orbit Control System (AOCS) and Guidance, Navigation, and Control (GNC), the challenges associated with spinning spacecraft missions primarily stem from the influence of centrifugal stiffening on the dynamics of the satellite's flexible rotating booms. Consequently,

the success of such missions is heavily dependent on the ability to design an accurate system model. In this regard, the comprehensive modeling of complex multibody structures becomes imperative, facilitating the early prediction of worst-case scenarios and providing the capability to push the control system to its performance limits. Moreover, having a model that is valid for any possible configuration simplifies the synthesis of the controller, eliminating the need for frequent transitions between control modes. Indeed, the transition between different control phases poses a critical aspect in control design, often involving intermediate tranquilization time windows.

The main contribution of this paper is to propose an adaptive control strategy for a spinning spacecraft that can robustly meet the required pointing performances, where the controller is gain-scheduled with respect to the angular velocity of the spinning spacecraft. The satellite's design is inspired by the THOR and Cluster missions, where the main equipment platform is located around a central rigid body. Two flexible booms, resembling long rods, are connected to the rigid hub of the spacecraft. These booms become active when the spacecraft starts spinning. Their purpose can be to measure the varying electrical and magnetic fields surrounding the spacecraft (Cluster mission) or to carry plasma measurement instruments at their tips (THOR project). In this paper, these measurement instruments will be treated as tip masses. Furthermore, it should also be noted that all the dynamic models of the different bodies that are used in this paper have been computed in [6].

The proposed model is built using the Two-Input-Two-Output Port (TITOP) approach [7], which considers forces and accelerations at the connection points as inputs and outputs. In contrast to conventional techniques, this method does not depend on particular boundary conditions at the connection points of the link. By integrating direct and inverse dynamic models in a concise state-space representation, the TITOP model ensures invertible input-output channels. This enables smooth incorporation into the overall multibody system model, treating it as a block-diagram model. Moreover, this approach provides the capability to represent complex multibody mechanical systems, preserving the uncertain characteristics of the plant and condensing all potential mechanical configurations into a single Linear Fractional Representation (LFR). The TITOP model effectively bridges the gap between the transfer matrix method and the effective mass-inertia method. This approach has been previously introduced in [8] and has found practical applications in space engineering, as demonstrated in [9–12]. The obtained LFR model is characterized by its parameterization with respect to the angular velocity, resulting in a Linear Parameter-Varying (LPV) system that accommodates the centrifugal stiffening effect affecting the dynamic behavior of the spacecraft's flexible booms.

The models constructed using the TITOP approach are well-suited for robust control synthesis, as well as robust performance assessment. Additionally, all the models developed with the TITOP approach have been integrated into the most recent release of the Satellite Dynamics Toolbox library (SDTlib) [13].

In this context, this paper presents a comprehensive approach for designing a spinning spacecraft mission scenario from an end-to-end perspective, taking into account the structure and control aspects. The authors aim to consider the challenges of flexibility, system uncertainty and time-varying dynamics in the design of a robust controller for a spinning spacecraft. As operations of large and flexible structures become more common in future space missions, this approach is increasingly relevant for ensuring the success of these kinds of scenarios.

2 The TITOP approach with motion vectors

The link $\mathcal{A}_i$ connected to the parent substructure $\mathcal{A}_{i-1}$ at the point P_i and to the child substructure $\mathcal{A}_{i+1}$ at the point C_i is depicted in Fig. 1a. The TITOP approach that has been previously presented in [7–12, 14] links the 6 components of the interaction wrenches to the 6 components of the inertial acceleration dual vectors at the points P_i and C_i, assuming small motions around null equilibrium conditions. To linearize the model of a spinning satellite around non-null kinematic equilibrium conditions ($\overline{\mathbf{v}}_{P_i}^{\mathcal{A}_i}$ and

$\overline{\boldsymbol{\omega}}_{P_i}^{\mathcal{A}_i}$), the TITOP model developed hereafter considers the 18-components motion vectors $\mathbf{m}_{P_i}^{\mathcal{A}_i}$ and $\mathbf{m}_{C_i}^{\mathcal{A}_i}$, as defined in the nomenclature, as well as their corresponding equilibrium values and variations. For example, it follows that:

$$\mathbf{m}_{P_i}^{\mathcal{A}_i} = \underbrace{\left[\mathbf{0}_{1\times6}, \mathbf{0}_{1\times6}, \overline{\mathbf{v}}_{P_i}^{\mathcal{A}_i^{\mathrm{T}}}, \overline{\boldsymbol{\omega}}_{P_i}^{\mathcal{A}_i^{\mathrm{T}}}, \overline{\mathbf{x}}_{P_i}^{\mathcal{A}_i^{\mathrm{T}}}, \overline{\boldsymbol{\Theta}}_{P_i}^{\mathcal{A}_i^{\mathrm{T}}}\right]^{\mathrm{T}}}_{\overline{\mathbf{m}}_{P_i}^{\mathcal{A}_i}} + \underbrace{\left[\delta\dot{\mathbf{v}}_{P_i}^{\mathcal{A}_i^{\mathrm{T}}}, \delta\dot{\boldsymbol{\omega}}_{P_i}^{\mathcal{A}_i^{\mathrm{T}}}, \delta\mathbf{v}_{P_i}^{\mathcal{A}_i^{\mathrm{T}}}, \delta\boldsymbol{\omega}_{P_i}^{\mathcal{A}_i^{\mathrm{T}}}, \delta\mathbf{x}_{P_i}^{\mathcal{A}_i^{\mathrm{T}}}, \delta\boldsymbol{\Theta}_{P_i}^{\mathcal{A}_i^{\mathrm{T}}}\right]^{\mathrm{T}}}_{\delta\mathbf{m}_{P_i}^{\mathcal{A}_i}} \tag{1}$$

Similarly, since the wrench $\overline{\mathbf{W}}_{\mathcal{A}_{i+1}/\mathcal{A}_i,C_i}$ applied at the point C_i at the equilibrium is no longer null, the linear TITOP model must now consider the deformed body frame $\mathcal{R}_{a_i(C_i)}$ attached to the body $\mathcal{A}_i$ at the point C_i, in addition to the "rigid" body frame $\mathcal{R}_{a_i}$ attached to the body $\mathcal{A}_i$ at the point P_i, as depicted in Fig. 1a.

Therefore, the double-port or TITOP model $\left[\mathfrak{T}_{P_iC_i}^{\mathcal{A}_i}(\mathrm{s})\right]_{\mathcal{R}_{a_i}}$ of the body $\mathcal{A}_i$ is a linear dynamic model between 24 inputs:

- the six components of the wrench variation $\left[\delta\mathbf{W}_{\mathcal{A}_{i+1}/\mathcal{A}_i,C}\right]_{\mathcal{R}_{a_i(C_i)}}$ applied by the child substructure $\mathcal{A}_{i+1}$ to the body $\mathcal{A}_i$ at the point C_i, expressed in the deformed body frame $\mathcal{R}_{a_i(C_i)}$.
- the eighteen components of the motion vector variation $\left[\delta\mathbf{m}_{P_i}^{\mathcal{A}_i}\right]_{\mathcal{R}_{a_i}}$ defined at the point P_i and expressed in the rigid body frame $\mathcal{R}_{a_i}$.

and 24 outputs:

- the eighteen components of the motion vector variation $\left[\delta\mathbf{m}_{C_i}^{\mathcal{A}_i}\right]_{\mathcal{R}_{a_i(C_i)}}$ defined at the point C_i and expressed in the deformed body frame $\mathcal{R}_{a_i(C_i)}$.
- the six components of the wrench variation $\left[\delta\mathbf{W}_{\mathcal{A}_i/\mathcal{A}_{i-1},P_i}\right]_{\mathcal{R}_{a_i}}$ that is applied by the body $\mathcal{A}_i$ to the parent substructure $\mathcal{A}_{i-1}$ at the point P_i, expressed in the rigid body frame $\mathcal{R}_{a_i}$.

and can be represented by the block-diagram depicted in Fig. 1b. The TITOP model is composed of the direct dynamic model (transfer from motion vector variation to wrench variation) at the point P_i and the inverse dynamic model (transfer from wrench variation to motion vector variation) at the point C_i. This model depends on the kinematic equilibrium conditions $\left[\overline{\mathbf{v}}_{P_i}^{\mathcal{A}_i^{\mathrm{T}}}, \overline{\boldsymbol{\omega}}_{P_i}^{\mathcal{A}_i^{\mathrm{T}}}\right]_{\mathcal{R}_{a_i}}^{\mathrm{T}}$ at the point P_i and the equilibrium wrench at the point C_i $\left[\overline{\mathbf{W}}_{\mathcal{A}_{i+1}/\mathcal{A}_i,C_i}\right]_{\mathcal{R}_{a_i(C_i)}} = \left[\overline{\mathbf{W}}_{\mathcal{A}_{i+1}/\mathcal{A}_i,C_i}\right]_{\mathcal{R}_{a_i}}$. Indeed, considering that the static deformations of flexible beams due to centrifugal loads are small and neglected in the computation of the equilibrium conditions, the frames $\mathcal{R}_{a_i}$ and $\mathcal{R}_{a_i(C_i)}$ are aligned. It should also be noted that the equilibrium conditions can be propagated forward (from parent to child) to provide $\left[\overline{\mathbf{v}}_{C_i}^{\mathcal{A}_i^{\mathrm{T}}}, \overline{\boldsymbol{\omega}}_{C_i}^{\mathcal{A}_i^{\mathrm{T}}}\right]_{\mathcal{R}_{a_i}}^{\mathrm{T}}$ and backwards (from child to parent) to provide $\left[\overline{\mathbf{W}}_{\mathcal{A}_i/\mathcal{A}_{i-1},P_i}\right]_{\mathcal{R}_{a_i}}$.

Moreover, Eq. (1) also introduced the geometric equilibrium conditions $\left[\overline{\mathbf{x}}_{P_i}^{\mathcal{A}_i^{\mathrm{T}}}, \overline{\boldsymbol{\Theta}}_{P_i}^{\mathcal{A}_i^{\mathrm{T}}}\right]_{\mathcal{R}_{a_i}}^{\mathrm{T}}$. However, the dynamics of the various TITOP models developed hereafter do not depend on these geometric conditions. For this reason, they do not appear on the block-diagram depicted in Fig. 1b.

Ultimately, the subscript i will be ommitted hereafter and the substructures (parent or child) connected to the body in question will be denoted as $\bullet$ for brevity. Similarly, the equilibrium signals (represented in

green in Fig. 1b) will not be displayed in the block-diagrams presented henceforth. For a more detailed explanation of the TITOP approach with motion vectors, the readers are encouraged to refer to [6].

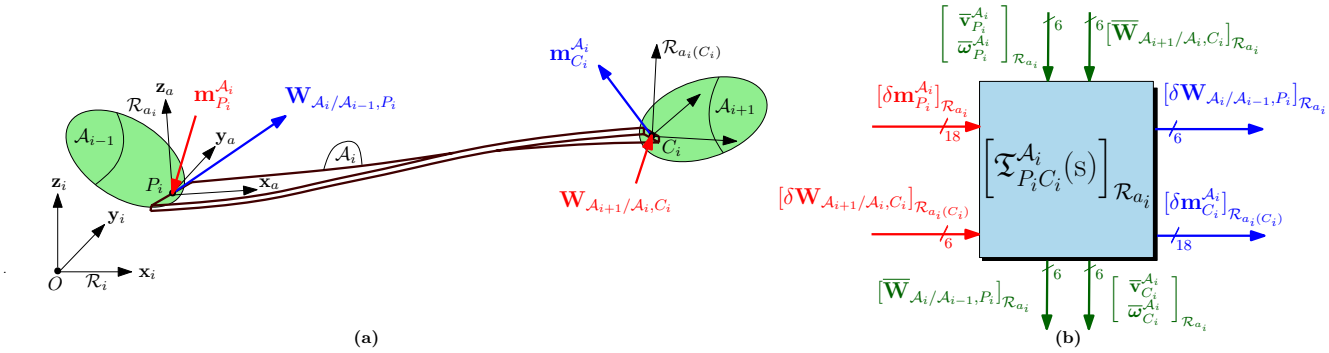

Fig. 1 (a) Three-Dimensional (3D) representation of a flexible spinning beam $\mathcal{A}_i$. (b) TITOP model $\left[\mathfrak{T}^{\mathcal{A}_i}_{P_iC_i}(\mathrm{s})\right]_{\mathcal{R}_{a_i}}$ block-diagram.

3 Case study: Spinning and flexible spacecraft

In the investigation of plasma characteristics in space, in-situ plasma measurements serve as a very important tool. Spinning spacecraft platforms are commonly employed for conducting such measurements due to their numerous advantages. One key benefit of utilizing a spinning spacecraft lies in its ability to consistently sample the plasma surroundings. Through rotation, the spacecraft allows the plasma instruments to capture plasma properties in all directions, leading to a more comprehensive understanding of the plasma environment [4]. Another advantage is the spinning spacecraft's capability to mitigate spacecraft charging effects. Stationary spacecraft can accumulate a negative charge due to electron buildup on its surface, disrupting in-situ plasma measurements by repelling the plasma. Nonetheless, when a spacecraft spins, the charge is more evenly distributed across its surface, reducing the overall charging effect. Additionally, spinning spacecraft platforms contribute to reducing instrument noise, which can originate from sources like electromagnetic interference and thermal fluctuations. The rotation of the spacecraft allows noise to be averaged out, resulting in more precise and reliable measurements.

3.1 Complete model of the system

For the mission scenario being studied in this paper, a spinning spacecraft is considered, as depicted in Fig. 2, where the shape of the spacecraft is inspired by the THOR and Cluster missions. The central cylinder $\mathcal{B}$ represents the main equipment platform. Furthermore, two long rod-shaped and flexible booms $\mathcal{A}_\bullet$ are attached to the rigid hub of the spacecraft $\mathcal{B}$ and operate when the spacecraft begins to spin. Their function can involve the measurement of fluctuating electrical and magnetic fields in the vicinity of the spacecraft, as demonstrated in the Cluster mission. Alternatively, they may serve as carriers for plasma measurement instruments located at their tips, as exemplified in the THOR project. Within the scope of this paper, the primary focus will be directed towards the second scenario, where the measurement instruments will be modeled as tip masses.

A detailed block-diagram representation of the complete system is also displayed in Fig. 2, where $\left[\mathfrak{T}^{\mathcal{A}_\bullet}_{P_\bullet C_\bullet}(\mathrm{s})\right]_{\mathcal{R}_{a_\bullet}}$ are the TITOP models of the flexible booms, $\left[\mathfrak{X}^{\mathcal{B}}_{GP_1P_2}(\mathrm{s})\right]_{\mathcal{R}_b}$ the model of the central rigid hub and $\left[\mathfrak{R}^{\mathcal{S}_\bullet}_{C_\bullet}(\mathrm{s})\right]_{\mathcal{R}_{s_\bullet}}$ the models of the tip masses located at the tips of the flexible booms. For a more detailed explanation of how these linearized models are calculated, the readers are encouraged to refer to [6]. Furthermore, the rotation matrices $\mathbf{P}^{\bullet}_{\mathcal{R}_\bullet/\mathcal{R}_\bullet}$ are described in Appendix A.

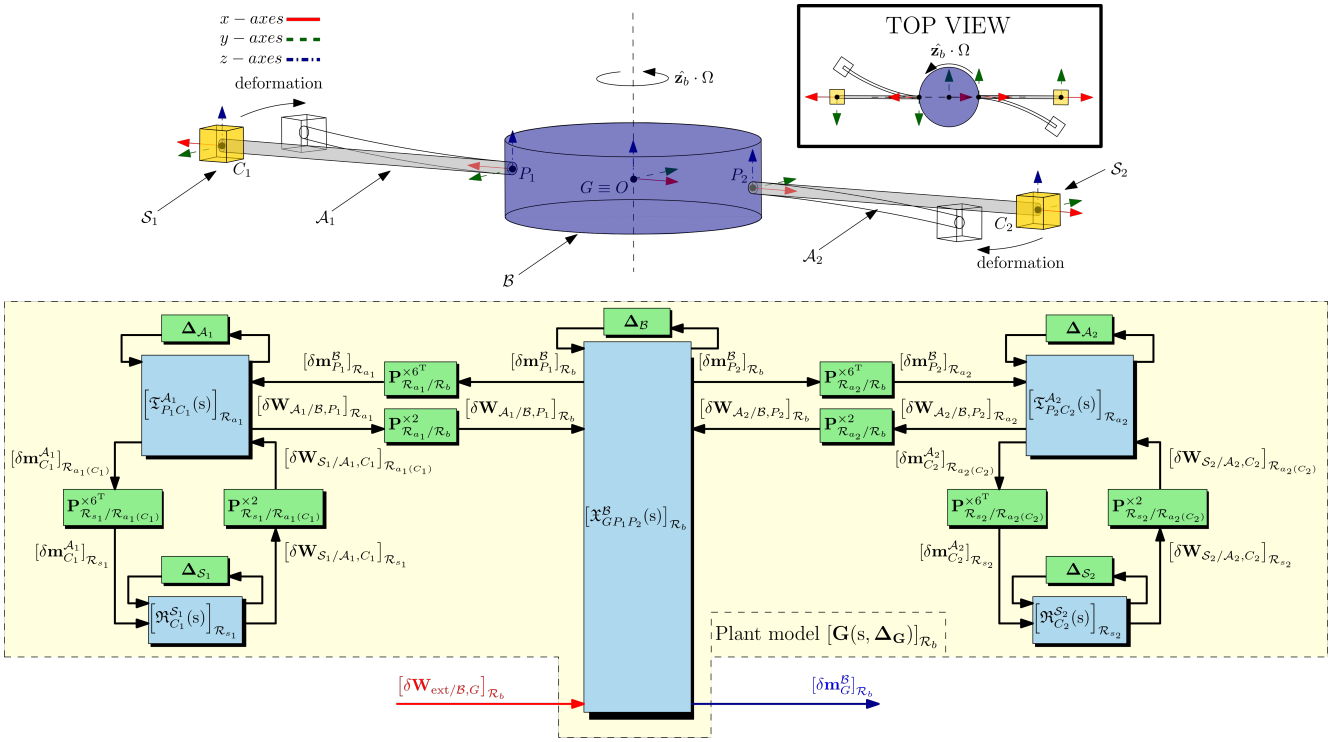

Fig. 2 3D representation and detailed block-diagram representation of a spinning satellite mission scenario composed of one main rigid body, two flexible booms and two tip masses representing two measurement instruments attached to the tip of each boom (Note: for the sake of simplicity, the x-axes are displayed in solid red lines, the y-axes in dashed green lines and the z-axes in dash-dotted blue lines).

In the case of spinning satellites, stability is observed in rotations around the principal axes aligned with the largest and smallest moments of inertia. Nonetheless, the rotation around the axis associated with the intermediate principal moment of inertia is unstable. This instability results in unexpected rotations, giving rise to a phenomenon widely recognized as the Dzhanibekov effect [15]. For this reason, it must be ensured that the rotation axis of the spacecraft does not correspond to the intermediate principal moment of inertia. In this particular scenario, the assumption is made that the spacecraft exclusively rotates around the $\mathbf{z}_b$-axis of its body frame $\mathcal{R}_b$ (without loss of generality), which corresponds to the largest moment of inertia (see Table 1). Consequently, it is considered that $\overline{\omega}^{\bullet}_{\bullet} = [0, 0, \Omega]^{\mathrm{T}}$. Moreover, spinning spacecraft undergo spin-up maneuvers, where the objective is to accelerate the system into the prescribed spinning motion and then maintain the expected angular velocity. Hence, the complete spacecraft system is parameterized according to the angular velocity $\Omega \in [0, 1]$ rad s^{-1}, where the selection of the variation range is based on the typical angular velocities achieved in missions of this kind.

Rayleigh damping: Rayleigh damping, also known as proportional damping or classical damping model, expresses damping as a linear combination of the mass and stiffness matrices, that is:

$$\mathbf{C} = \alpha\mathbf{M} + \beta\mathbf{K} \tag{2}$$

where α and β are real scalars and $\mathbf{M}$, $\mathbf{C}$ and $\mathbf{K}$ are the mass, damping and stiffness matrices of a certain dynamic system. The procedure introduced by Hall [16] is convenient for determining α and β. In order to use it, one has to select a desired amount of damping ξ and a frequency range covering all the modes of interest from ϖ to $R\varpi$, with $R > 1$. Then, the bounds on the damping ratios that are assigned to these modes within the specified frequency range can be computed. First, let us define Δ_ξ as follows:

Table 1 Spinning spacecraft mechanical data and equilibrium conditions.

	Parameter	Description	Value
Central rigid body $\mathcal{B}$	$\overline{\mathbf{GP}}_{\bullet}$	distance vector between G and $P_{\bullet}$ in equilibrium and written in $\mathcal{R}_b$	$[\pm 2, 0, 0]$ m
	$m^{\mathcal{B}}$	mass of $\mathcal{B}$	$500 \pm 5\%$ kg
	$\begin{bmatrix} J^{\mathcal{B}}_{xx} & J^{\mathcal{B}}_{xy} & J^{\mathcal{B}}_{xz} \\ & J^{\mathcal{B}}_{yy} & J^{\mathcal{B}}_{yz} \\ & & J^{\mathcal{B}}_{zz} \end{bmatrix}$	inertia of $\mathcal{B}$ computed at the point G and written in $\mathcal{R}_b$	$\begin{bmatrix} 570.42 \pm 5\% & 0 & 0 \\ & 570.42 \pm 5\% & 0 \\ & & 1000 \pm 5\% \end{bmatrix}$ kg m^2
	$\mathcal{T}_{\mathcal{R}_{a_1}/\mathcal{R}_b}$	change of frame DCM between $\mathcal{R}_{a_1}$ and $\mathcal{R}_b$	$\begin{bmatrix} -1 & 0 & 0 \\ 0 & -1 & 0 \\ 0 & 0 & 1 \end{bmatrix}$
	$\mathcal{T}_{\mathcal{R}_{a_2}/\mathcal{R}_b}$	change of frame DCM between $\mathcal{R}_{a_2}$ and $\mathcal{R}_b$	$\mathbf{I}_3$
	$\overline{\mathbf{v}}^{\mathcal{B}}_{G}$	inertial velocity vector of the body $\mathcal{B}$ computed at the point G in equilibrium	$\mathbf{0}_{3\times 1}$ m s^{-1}
	$\overline{\boldsymbol{\omega}}^{\mathcal{B}}_{G}$	angular velocity vector of the body $\mathcal{B}$ computed at the point G in equilibrium	$[0, 0, \Omega \in [0, 1]]^{\mathrm{T}}$ rad s^{-1}
Flexible booms $\mathcal{A}_{\bullet}$	$l^{\mathcal{A}_{\bullet}}$	length of $\mathcal{A}_{\bullet}$	50 m
	$\rho^{\mathcal{A}_{\bullet}}$	mass density of $\mathcal{A}_{\bullet}$	2700 kg m^{-3}
	$S^{\mathcal{A}_{\bullet}}$	cross-sectional area of $\mathcal{A}_{\bullet}$	3.14×10^{-4} m^2
	$E^{\mathcal{A}_{\bullet}}$	Young's modulus of $\mathcal{A}_{\bullet}$	7×10^{10} N m^{-2}
	$\nu^{\mathcal{A}_{\bullet}}$	Poisson's ratio of $\mathcal{A}_{\bullet}$	0.33
	$J^{\mathcal{A}_{\bullet}}_{px}$	second polar moment of area of $\mathcal{A}_{\bullet}$ with respect to the $\mathbf{x}_a$-axis	1.57×10^{-8} m^4
	$J^{\mathcal{A}_{\bullet}}_{y}$	second moment of area of $\mathcal{A}_{\bullet}$ with respect to the $\mathbf{y}_a$-axis	7.85×10^{-9} m^4
	$J^{\mathcal{A}_{\bullet}}_{z}$	second moment of area of $\mathcal{A}_{\bullet}$ with respect to the $\mathbf{z}_a$-axis	7.85×10^{-9} m^4
	$\mathcal{T}_{\mathcal{R}_{s_{\bullet}}/\mathcal{R}_{a_{\bullet}(C_{\bullet})}}$	change of frame DCM between $\mathcal{R}_{s_{\bullet}}$ and $\mathcal{R}_{a_{\bullet}(C_{\bullet})}$	$\mathbf{I}_3$
	$\overline{\mathbf{x}}^{\mathcal{A}_{\bullet}}_{P_{\bullet}}$	distance vector between O and $P_{\bullet}$ in equilibrium and written in $\mathcal{R}_{a_{\bullet}}$	$[r = 2, 0, 0]^{\mathrm{T}}$ m
	$\overline{\boldsymbol{\Theta}}^{\mathcal{A}_{\bullet}}_{P_{\bullet}}$	Euler angles of the beam $\mathcal{A}_{\bullet}$ computed at the point $P_{\bullet}$ in equilibrium	$\mathbf{0}_{3\times 1}$ rad
	$\overline{\mathbf{v}}^{\mathcal{A}_{\bullet}}_{P_{\bullet}}$	inertial velocity vector of the beam $\mathcal{A}_{\bullet}$ computed at the point $P_{\bullet}$ in equilibrium	$[0, r\Omega, 0]^{\mathrm{T}}$ m s^{-1}
	$\overline{\boldsymbol{\omega}}^{\mathcal{A}_{\bullet}}_{P_{\bullet}}$	angular velocity vector of the beam $\mathcal{A}_{\bullet}$ computed at the point $P_{\bullet}$ in equilibrium	$[0, 0, \Omega \in [0, 1]]^{\mathrm{T}}$ rad s^{-1}
	$\overline{\mathbf{W}}_{\mathcal{S}_{\bullet}/\mathcal{A}_{\bullet},C_{\bullet}}$	wrench vector applied by the body $\mathcal{S}_{\bullet}$ to the body $\mathcal{A}_{\bullet}$ at the point $C_{\bullet}$ in equilibrium	$\left[m^{\mathcal{S}_{\bullet}}\left(l^{\mathcal{A}_{\bullet}} + r\right)\Omega^2, 0, 0, 0, 0, 0\right]^{\mathrm{T}}$ [N, N m]
Tip masses $\mathcal{S}_{\bullet}$	$m^{\mathcal{S}_{\bullet}}$	mass of $\mathcal{S}_{\bullet}$	5 kg
	$\begin{bmatrix} J^{\mathcal{S}_{\bullet}}_{xx} & J^{\mathcal{S}_{\bullet}}_{xy} & J^{\mathcal{S}_{\bullet}}_{xz} \\ & J^{\mathcal{S}_{\bullet}}_{yy} & J^{\mathcal{S}_{\bullet}}_{yz} \\ & & J^{\mathcal{S}_{\bullet}}_{zz} \end{bmatrix}$	inertia of $\mathcal{S}_{\bullet}$ computed at the point $C_{\bullet}$ and written in $\mathcal{R}_{s_{\bullet}}$	$\begin{bmatrix} 0 & 0 & 0 \\ & 0 & 0 \\ & & 0 \end{bmatrix}$ kg m^2
	$\overline{\mathbf{v}}^{\mathcal{S}_{\bullet}}_{C_{\bullet}}$	inertial velocity vector of the beam $\mathcal{S}_{\bullet}$ computed at the point $C_{\bullet}$ in equilibrium	$\left[0, \left(l^{\mathcal{A}_{\bullet}} + r\right)\Omega, 0\right]^{\mathrm{T}}$ m s^{-1}
	$\overline{\boldsymbol{\omega}}^{\mathcal{S}_{\bullet}}_{C_{\bullet}}$	angular velocity vector of the body $\mathcal{S}_{\bullet}$ computed at the point $C_{\bullet}$ in equilibrium	$[0, 0, \Omega \in [0, 1]]^{\mathrm{T}}$ rad s^{-1}

$$\Delta_{\xi} = \xi \frac{1 + R - 2\sqrt{R}}{1 + R + 2\sqrt{R}} \tag{3}$$

The modes in the given frequency range $[\varpi, R\varpi]$ will have a damping ratio bounded by $\xi_{\max} = \xi + \Delta_{\xi}$ and $\xi_{\min} = \xi - \Delta_{\xi}$. Ultimately, α and β can be calculated from:

$$\alpha = 2\xi\varpi \frac{2R}{1 + R + 2\sqrt{R}} \quad \text{and} \quad \beta = 2\xi \frac{1}{\varpi} \frac{2}{1 + R + 2\sqrt{R}} \tag{4}$$

Within the scope of this specific application, taking into account the variability in Ω and the characteristics of the flexible booms, the parameters are specified in the following manner: $\varpi = 3.58 \times 10^{-2}$ rad s^{-1}, $\xi = 0.01$ and $R = 26.7318$. Following the notation presented in [6], the new damping matrix of the bodies $\mathcal{A}_{\bullet}$ is equal to $\mathbf{C} = \alpha\mathbf{M}_{ff} + \beta\mathbf{K}_{ff}$. Ultimately, the matrix $\mathbf{C}$ must be added to the matrix $\mathbf{D}_{ff}$ in [6], so that the new damping contributions are taken into account on the state-space representations of the flexible booms.

By considering the damping matrix $\mathbf{C}$, the angular velocity varying parameter Ω appears 8, 221 and 4 times in the models of the bodies $\mathcal{B}$, $\mathcal{A}_{\bullet}$ and $\mathcal{S}_{\bullet}$, respectively. It should also be noted that the number of computed occurrences for the varying parameter Ω depends on the equilibrium conditions computation of the system. In this case, the number of occurrences of Ω corresponds to the spinning satellite mission scenario displayed in Fig. 2. For the flexible boom models, it is considered that $\overline{\mathbf{x}}^{\mathcal{A}_{\bullet}}_{P_{\bullet}} = [r, 0, 0]^{\mathrm{T}}$, $\overline{\boldsymbol{\Theta}}^{\mathcal{A}_{\bullet}}_{P_{\bullet}} = \mathbf{0}_{3\times 1}$ and $\overline{\boldsymbol{\omega}}^{\mathcal{A}_{\bullet}}_{P_{\bullet}} = [0, 0, \Omega]^{\mathrm{T}}$. For this reason, it can be concluded that $\overline{\mathbf{W}}_{\mathcal{S}_{\bullet}/\mathcal{A}_{\bullet},C_{\bullet}} =$

$\left[m^{\mathcal{S}_\bullet}\left(l^{\mathcal{A}_\bullet}+r\right)\Omega^2, 0, 0, 0, 0, 0\right]^{\mathrm{T}}$, where $m^{\mathcal{S}_\bullet}$ are the tip mass values located at the points $C_\bullet$ and $l^{\mathcal{A}_\bullet}$ represents the lengths of the beams $\mathcal{A}_\bullet$. Due to the spinning motion, it can also be inferred that $\overline{\mathbf{v}}^{\mathcal{A}_\bullet}_{P_\bullet} = [0, r\Omega, 0]^{\mathrm{T}}$. These equilibrium conditions are expressed in the body frames $\mathcal{R}_{a_\bullet}$, which are the frames of reference used to define the beam models. A similar procedure can be carried out for the computation of $\overline{\mathbf{v}}^{\mathcal{A}_\bullet}_{C_\bullet}$, with $\overline{\mathbf{v}}^{\mathcal{A}_\bullet}_{C_\bullet} = \left[0, \left(l^{\mathcal{A}_\bullet}+r\right)\Omega, 0\right]^{\mathrm{T}}$.

Mechanical uncertainty $\boldsymbol{\Delta}_{\mathrm{mec}}$: One of the objectives of this paper is to demonstrate how to design a controller in the presence of model uncertainty. For this reason, relative uncertainty is taken into account on the mass and moments of inertia of $\mathcal{B}$, since the robust stability and performance of the spinning spacecraft need to be ensured even when the mechanical characteristics of the central rigid hub are not perfectly known. As an example, let us now consider the mass of the central rigid body $m^{\mathcal{B}}$ as uncertain:

$$m^{\mathcal{B}} = m_0^{\mathcal{B}}(1 + r_{m^{\mathcal{B}}}\delta_{m^{\mathcal{B}}}) \tag{5}$$

where $m_0^{\mathcal{B}}$ is the body's nominal mass, $r_{m^{\mathcal{B}}}$ is used to set the maximum percent of variation for the body's mass and $\delta_{m^{\mathcal{B}}} \in [-1, 1]$ is a normalized real uncertainty. In this case, $\delta_{m^{\mathcal{B}}}$ appears five times in the LFR of the body $\mathcal{B}$. Similarly, relative uncertainty is considered on the inertial properties of $\mathcal{B}$. However, only the diagonal moments of inertia are assumed to be uncertain while the off-diagonal terms are kept at their nominal values. For the moments of inertia of the rigid body $\mathbf{J}^{\mathcal{B}}_{xx}$, $\mathbf{J}^{\mathcal{B}}_{yy}$ and $\mathbf{J}^{\mathcal{B}}_{zz}$, the normalized real uncertainties $\delta_{\mathbf{J}^{\mathcal{B}}_{xx}}$ and $\delta_{\mathbf{J}^{\mathcal{B}}_{yy}}$ have two occurrences in the same LFR, while $\delta_{\mathbf{J}^{\mathcal{B}}_{zz}}$ only appears once. Furthermore, $\delta_{\mathbf{J}^{\mathcal{B}}_{\bullet}} \in [-1, 1]$ and $r_{\mathbf{J}^{\mathcal{B}}_{\bullet}}$ are used to set the maximum percent of variation for $\mathbf{J}^{\mathcal{B}}_{\bullet}$, just like in Eq. (5). Therefore, the mechanical uncertainty block of the body $\mathcal{B}$ can be written as $\boldsymbol{\Delta}_{\mathrm{mec}} = \mathrm{diag}\left(\delta_{m^{\mathcal{B}}}\mathbf{I}_5, \delta_{\mathbf{J}^{\mathcal{B}}_{xx}}\mathbf{I}_2, \delta_{\mathbf{J}^{\mathcal{B}}_{yy}}\mathbf{I}_2, \delta_{\mathbf{J}^{\mathcal{B}}_{zz}}\right)$. All the numerical values and range of variations of the numerous system parameters which are employed in this section are described in Table 1.

When the full system is assembled, a global LFR representation is obtained, which fully captures the dynamics and interactions between all the subsystems of the scenario being studied. Additionally, this model also takes into account the various uncertainty effects in a very compact representation. Fig. 2 illustrates the internal structure of the overall LFR model $[\mathbf{G}(\mathrm{s}, \boldsymbol{\Delta}_{\mathbf{G}})]_{\mathcal{R}_b}$, as well as the interconnections between the several subsystems. In this representation, all the block uncertainties are isolated at the component level, with $\boldsymbol{\Delta}_{\mathcal{B}} = \mathrm{diag}\left(\Omega\mathbf{I}_8, \boldsymbol{\Delta}_{\mathrm{mec}}\right)$, $\boldsymbol{\Delta}_{\mathcal{A}_\bullet} = \Omega\mathbf{I}_{221}$, $\boldsymbol{\Delta}_{\mathcal{S}_\bullet} = \Omega\mathbf{I}_4$ and $\boldsymbol{\Delta}_{\mathbf{G}} = \mathrm{diag}\left(\boldsymbol{\Delta}_{\mathcal{B}}, \boldsymbol{\Delta}_{\mathcal{A}_1}, \boldsymbol{\Delta}_{\mathcal{A}_2}, \boldsymbol{\Delta}_{\mathcal{S}_1}, \boldsymbol{\Delta}_{\mathcal{S}_2}\right)$. Finally, it should also be noted that it is crucial for a stable equilibrium to be established that the spacecraft exhibits symmetry around its spin axis $\mathbf{z}_b$.

3.2 Analysis of the spinning and flexible spacecraft dynamics

Let us now analyze the singular values of the spinning and flexible spacecraft model, given by $[\mathbf{G}(\mathrm{s}, \boldsymbol{\Delta}_{\mathbf{G}})]_{\mathcal{R}_b}$, for different values of Ω and considering $\boldsymbol{\Delta}_{\mathrm{mec}}$ nominal. For instance, if the transfer function from the second component of the external torque $\delta\mathbf{T}_{\mathrm{ext}/\mathcal{B},G}$ to the second component of the angular acceleration $\delta\dot{\boldsymbol{\omega}}^{\mathcal{B}}_{G}$ is considered, Fig. 3 shows how the natural frequencies of the system evolve with respect to Ω. As stated before, the centrifugal forces applied by the tip masses $\mathcal{S}_\bullet$ to the spinning beams $\mathcal{A}_\bullet$ are determined by the equation $\overline{\mathbf{W}}_{\mathcal{S}_\bullet/\mathcal{A}_\bullet,C_\bullet}\{1\} = m^{\mathcal{S}_\bullet}\left(l^{\mathcal{A}_\bullet}+r\right)\Omega^2$. These forces are projected onto the beams' body frames, labeled as $\mathcal{R}_{a_\bullet}$. They are also accountable for the centrifugal stiffening effect, which causes the natural frequencies of the system to shift to the right in the singular values plots as the value of Ω increases, as displayed in Fig. 3.

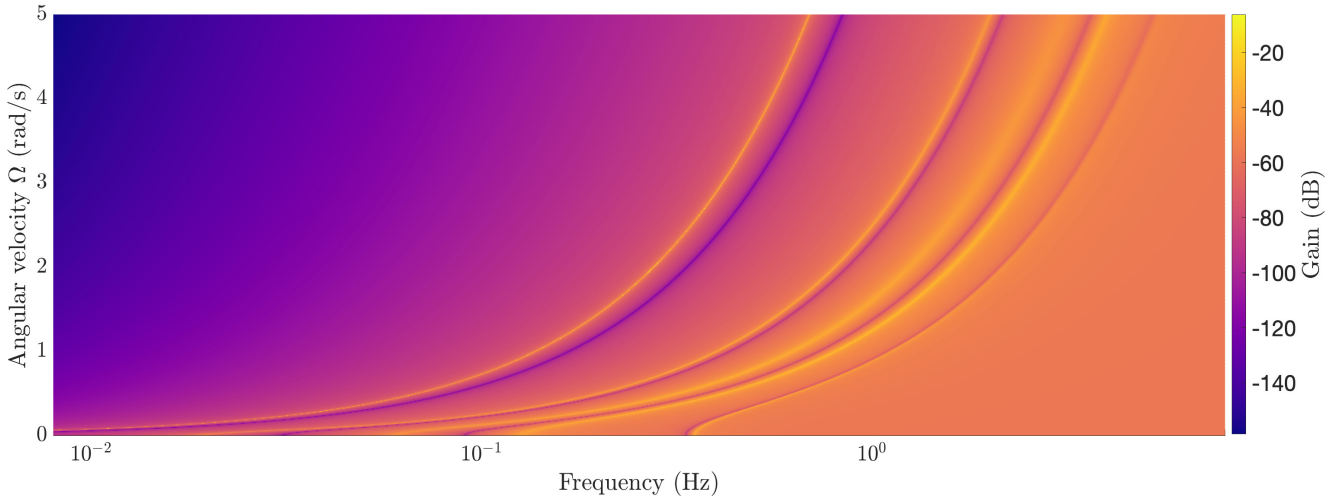

Fig. 3 Singular values of the model $[\mathbf{G}(\mathrm{s}, \boldsymbol{\Delta}_{\mathbf{G}})]_{\mathcal{R}_b}$ with respect to the angular velocity Ω and along a dense grid of frequencies ($\delta\mathbf{T}_{\mathrm{ext}/\mathcal{B},G}\{2\} \rightarrow \delta\dot{\boldsymbol{\omega}}_G^{\mathcal{B}}\{2\}$ channel).

4 Control architecture and synthesis methodology

Some of the challenges of a spinning spacecraft mission scenario include the control structure interactions between the flexible appendages and the AOCS, the system uncertainties, the flexible dynamics and the dynamic couplings.

4.1 Gain-scheduled $\mathcal{H}_\infty$ control

In order to design a control law that accommodates the desired performance requirements, the synthesis problem is recast into the nonsmooth $\mathcal{H}_\infty$ framework [17] by first assembling the weighted interconnection shown in Fig. 4a. This model is used to design an LPV gain-scheduled controller [14, 18, 19], where the scheduling variable is the angular velocity $\boldsymbol{\Omega}$. A global uncertainty block system is built in a very straightforward way by just concatenating the individual uncertainty blocks, where the global block is defined as $\boldsymbol{\Omega}\mathbf{I}_{458}$. The plant model $\mathbf{G}(\mathrm{s})$ is the one represented in Fig. 2. However, only the minimal realization corresponding to the channels $\delta\mathbf{T}_{\mathrm{ext}/\mathcal{B},G} \rightarrow \left[\delta\boldsymbol{\omega}_G^{\mathcal{B}^{\mathrm{T}}}, \delta\phi_G^{\mathcal{B}}, \delta\theta_G^{\mathcal{B}}\right]^{\mathrm{T}}$ is considered, with $\delta\boldsymbol{\Theta}_G^{\mathcal{B}} = \left[\delta\phi_G^{\mathcal{B}}, \delta\theta_G^{\mathcal{B}}, \delta\psi_G^{\mathcal{B}}\right]^{\mathrm{T}}$, since the objective is to design an attitude controller. This interconnection is composed of the following blocks:

Sensor and actuator models: First, the star tracker dynamics $\mathbf{G}_{\mathcal{SST}}(\mathrm{s})$ correspond to a first order low pass filter with a cutoff frequency of 8 Hz. Secondly, the gyroscope dynamics $\mathbf{G}_{\mathcal{GYRO}}(\mathrm{s})$ are represented by a first order low pass filter with a 200 Hz cutoff frequency. Finally, the reaction wheel system dynamics $\mathbf{G}_{\mathcal{RW}}(\mathrm{s})$ are approximated by a second order transfer, with a damping ratio equal to 0.7 and a natural frequency of 200 Hz.

Disturbance weights: The weight $\mathbf{W}_{\mathrm{ext}}(\mathrm{s}) = \mathrm{diag}\left(\frac{0.002577}{2.236s+0.2236}, \frac{0.009685}{2.236s+0.2236}, \frac{0.01239}{2.236s+0.2236}\right)$ N m is used to define an upper bound on the expected closed-loop orbital disturbances at different frequencies. These transfer functions are approximated from the power spectral density of the various torque disturbances that are expected to act on a spinning spacecraft mission like Cluster.

Performance weights: The purpose of the weight $\mathbf{W}_u = \mathrm{diag}\,(0.8333, 0.8333, 0.8333)$ $\mathrm{N}^{-1}\,\mathrm{m}^{-1}$ is to impose a desired closed-loop upper bound of 1.2 N m on the worst-case actuator signals at different frequencies. Similarly, the objective of the absolute pointing error (APE) requirement $\mathbf{W}_p = \mathrm{diag}\,(35.2113,\ 35.2113)$ rad^{-1} is to impose an upper bound of 0.0284 rad on the two different axes.

Roll-off filter: A 4th-order roll-off Butterworth filter $\mathbf{F}_{\text{ro}}(\text{s})$ with a cutoff frequency of 0.7 Hz is also added to the output control signal $\mathbf{u}$, ensuring the controller is not sensitive to high frequency content.

Finally, the structure that was chosen for the adaptable controller $\widehat{\mathbf{K}}_{\text{LPV}}(\text{s}, \Omega)$ is given by:

$$\widehat{\mathbf{K}}_{\text{LPV}}(\text{s}, \Omega) = \mathcal{F}_u \left(\left[\begin{array}{c|c} \mathbf{A}_{\mathbf{K}_0} & \mathbf{B}_{\mathbf{K}_0} \\ \hline \mathbf{C}_{\mathbf{K}_0} & \mathbf{D}_{\mathbf{K}_0} \end{array} \right] + \Omega \left[\begin{array}{c|c} \mathbf{A}_{\mathbf{K}_1} & \mathbf{B}_{\mathbf{K}_1} \\ \hline \mathbf{C}_{\mathbf{K}_1} & \mathbf{D}_{\mathbf{K}_1} \end{array} \right], \frac{\mathbf{I}_{n_c}}{\text{s}} \right) = \mathcal{F}_l \left(\mathbf{K}(\text{s}), \Omega \mathbf{I}_{n_k} \right) \tag{6}$$

with $\mathbf{K}(\text{s}) \subset \mathbb{RH}_\infty^{(n_k+n_y)\times(n_k+n_u)}$, where $\mathbb{RH}_\infty^{(n_k+n_y)\times(n_k+n_u)}$ represents the set of finite gain transfer matrices with $(n_k + n_y)$ outputs and $(n_k + n_u)$ inputs. Furthermore, n_c is the order of the controller, n_y is the number of inputs, n_u is the number of outputs, n_k is the number of occurrences of the scheduling parameter Ω, $\mathcal{F}_u(\cdot)$ represents the upper linear fractional transformation and $\mathcal{F}_l(\cdot)$ is the lower linear fractional transformation. In Eq. (6), the matrices $\mathbf{A}_{\mathbf{K}_0}, \mathbf{A}_{\mathbf{K}_1}, \mathbf{B}_{\mathbf{K}_0}, \mathbf{B}_{\mathbf{K}_1}, \mathbf{C}_{\mathbf{K}_0}, \mathbf{C}_{\mathbf{K}_1}, \mathbf{D}_{\mathbf{K}_0}, \mathbf{D}_{\mathbf{K}_1}$ are real matrices of appropriate dimensions. The closed-loop model, denoted $\mathbf{C}(\text{s}, \Omega)$, can be observed in Fig. 4b. Furthermore, the uncertain closed-loop model is given by $\widehat{\mathbf{C}}(\text{s}, \Omega, \mathbf{\Delta}_{\text{mec}}) = \mathcal{F}_u \left(\mathbf{C}(\text{s}, \Omega), \mathbf{\Delta}_{\text{mec}} \right)$. An $\mathcal{H}_\infty$ problem is solved, composed of two hard constraints. The first constraint is a requirement on the gain from the normalized orbital disturbances to the normalized APE and worst-case actuator signals, as follows:

$$\sup_{\mathbf{\Delta}_{\text{mec}}, \Omega} \left\| \widehat{\mathbf{C}}_{\mathbf{d}_u \to \tilde{\mathbf{e}}}(\text{s}, \Omega, \mathbf{\Delta}_{\text{mec}}) \right\|_\infty \leq 1 \quad \text{(hard constraint)} \text{, with} \quad \tilde{\mathbf{e}} = \left[\begin{array}{c} \mathbf{e}_u \\ \mathbf{e}_p \end{array} \right] \tag{7}$$

The second constraint is a requirement on the input sensitivity function, which is given by:

$$\frac{1}{\gamma} \sup_{\mathbf{\Delta}_{\text{mec}}, \Omega} \left\| \widehat{\mathbf{C}}_{\mathbf{d}_s \to \mathbf{e}_t}(\text{s}, \Omega, \mathbf{\Delta}_{\text{mec}}) \right\|_\infty \leq 1 \quad \text{(hard constraint)} \tag{8}$$

In Eq. (8), the upper bound on the input sensitivity function is equal to $\gamma = 1.5$, which ensures on the three different axes a modulus margin bigger than $\frac{1}{\gamma} = 0.667$, a gain margin bigger than $\frac{\gamma}{\gamma-1} = 3$ and a phase margin bigger than $2 \arcsin \frac{1}{2\gamma} = 38.9\,^\circ$. The matrix $\mathbf{D}_{\mathbf{K}_0}$ is initialized with a static baseline Proportional Derivative (PD) controller $\mathbf{K}_{\text{PD}}$ tuned to the total nominal inertia of the spinning spacecraft, as follows:

$$\mathbf{K}_{\text{PD}} = \left[\begin{array}{cc} \mathbf{k}_{\text{att}} & \mathbf{c}_{\text{att}} \end{array} \right] \quad \text{with} \quad \begin{cases} \mathbf{k}_{\text{att}} = \omega_{\text{att}}^2 \mathbf{J}_{\text{tot}(1:3,1:2)} \\ \mathbf{c}_{\text{att}} = 2\xi_{\text{att}} \omega_{\text{att}} \mathbf{J}_{\text{tot}} \end{cases} \tag{9}$$

where $\mathbf{J}_{\text{tot}}$ is the inertia tensor of the collection of all the body elements, computed at the point G and measured with respect to $\mathcal{R}_b$. The objective is to have a critically damped system that returns to rest slowly without oscillating when tracking the reference signals. For this reason, $\xi_{\text{att}} = 1$ and $\omega_{\text{att}} = 0.01$ Hz represent the controller's damping ratio and natural frequency, respectively. These values of ξ_{att} and ω_{att} are merely an initial tuning guess which were chosen to avoid overshoot and to achieve a large settling time. Furthermore, $\mathbf{A}_{\mathbf{K}_0}$, $\mathbf{B}_{\mathbf{K}_0}$, $\mathbf{C}_{\mathbf{K}_0}$ are initialized with null matrices of appropriate dimensions. The resulting controller $\widehat{\mathbf{K}}_{\text{LPV}}(\text{s}, \Omega)$ has $n_c = 3$ states and $n_k = 7$ occurrences of the parameter Ω.

Fig. 5 illustrates the singular values corresponding to the channels $\mathbf{d}_u \to \tilde{\mathbf{e}}$ and $\mathbf{d}_s \to \mathbf{e}_t$ for three distinct closed-loop systems. The controllers utilized to close the loop in these systems are represented by $\mathbf{K}_{\text{PD}}$, $\widehat{\mathbf{K}}_{\text{PD}}$ and $\widehat{\mathbf{K}}_{\text{LPV}}(\text{s}, \Omega)$. The matrix $\widehat{\mathbf{K}}_{\text{PD}}$ is a static controller and has the same structure as $\mathbf{K}_{\text{PD}}$. However, this controller is optimized by means of the $\mathcal{H}_\infty$ framework, considering the constraints specified in Eqs. (7) and (8). In Fig. 5, each nominal closed-loop system ($\mathbf{\Delta}_{\text{mec}}$ is not taken into account)

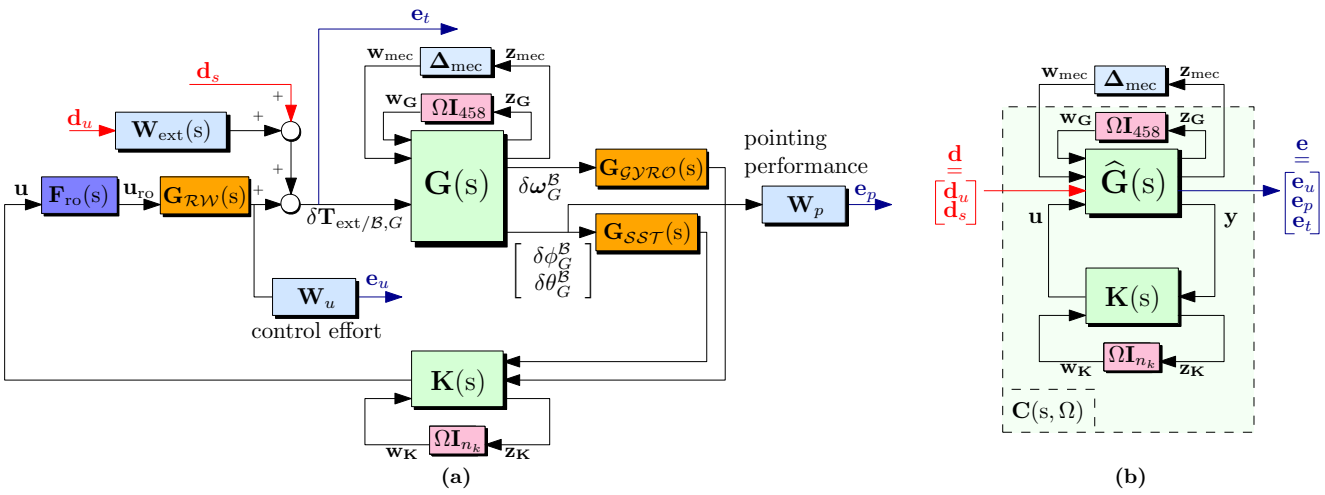

Fig. 4 (a) System architecture used for controller synthesis. (b) Equivalent standard form of the interconnection.

is parameterized according to several different values of Ω. Furthermore, the same figure also shows the gains of the worst-case scenarios provided by the MATLAB routine `systune` (worst combinations of uncertain parameters) for the uncertain closed-loop systems corresponding to the controllers $\widehat{\mathbf{K}}_{\mathrm{PD}}$ and $\widehat{\mathbf{K}}_{\mathrm{LPV}}(\mathrm{s},\Omega)$. These worst-case scenarios are linked to the worst-case configurations of Ω and $\boldsymbol{\Delta}_{\mathrm{mec}}$ for the two different uncertain closed-loop systems. For a better computation of the worst-cases, the structured singular value function $\mu_{\delta}(\cdot)$ should be used [20], which provides very precise information about the magnitude of uncertainty which is needed to destabilize the loop at any frequency.

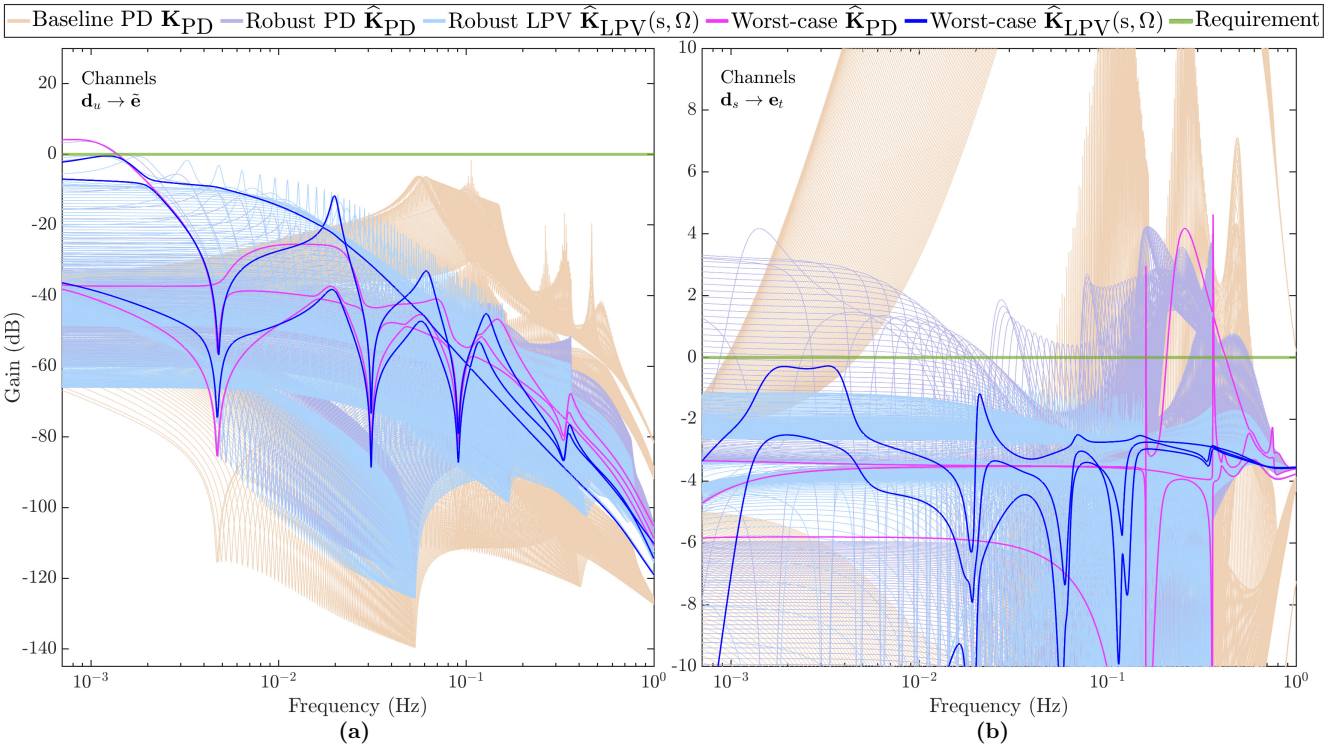

Fig. 5 Gains of three different nominal closed-loop systems corresponding to the controllers $\mathbf{K}_{\mathrm{PD}}$, $\widehat{\mathbf{K}}_{\mathrm{PD}}$ and $\widehat{\mathbf{K}}_{\mathrm{LPV}}(\mathrm{s},\Omega)$ for different values of Ω, as well as the worst-case singular values associated with the uncertain closed-loop systems corresponding to the controllers $\widehat{\mathbf{K}}_{\mathrm{PD}}$ and $\widehat{\mathbf{K}}_{\mathrm{LPV}}(\mathrm{s},\Omega)$: (a) Channels $\mathbf{d}_u \to \tilde{\mathbf{e}}$. (b) Channels $\mathbf{d}_s \to \mathbf{e}_t$.

It can be observed in Figs. 5a and 5b that, when the baseline controller $\mathbf{K}_{\text{PD}}$ is used, the gains of the corresponding closed-loop system do not comply with the requirement on the input sensitivity function at multiple frequencies. This is logical, as the baseline tuning method illustrated in Eq. (9) fails to consider disturbances and performance/stability constraints. Nevertheless, the design of the robust PD controller $\widehat{\mathbf{K}}_{\text{PD}}$ does take into account all the disturbances and requirements. Despite this, the gains of the corresponding closed-loop indicate that the imposed constraints are still not met when $\widehat{\mathbf{K}}_{\text{PD}}$ is used to close the loop. Indeed, the best achieved hard constraint values that are given by the MATLAB routine `systune` show exactly that for the design of $\widehat{\mathbf{K}}_{\text{PD}}$, since they are bigger than 1 for the two hard requirements shown in Eqs. (7) and (8). Finally, when the robust LPV controller $\widehat{\mathbf{K}}_{\text{LPV}}(\text{s}, \Omega)$ is used, the associated gains are always below 0 dB, meaning that the hard constraints imposed in Eqs. (7) and (8) are completely satisfied. From this analysis, it is possible to conclude that static PD controllers may prove inadequate for effectively controlling complex flexible systems with time-varying dynamics. Indeed, the only controller that meets all the requirements is the robust LPV controller.

Ultimately, the gains of $\mathbf{F}_{\text{ro}}(\text{s})\widehat{\mathbf{K}}_{\text{LPV}}(\text{s}, \Omega)$ are shown in Fig. 6 for the channels $\mathbf{y}\{2\} \rightarrow \mathbf{u}_{\text{ro}}$ and for different values of $\Omega \in [0, 1]$ rad s^{-1}. A behavior similar to that of a notch filter can be seen in the first and third plots. This behavior serves as a means for the controller to counteract problematic resonances caused by the system's flexible modes, which persist within the closed-loop system's bandwidth. For example, the described behavior occurs at the frequency equal to 0.068 Hz for the channel $\mathbf{y}\{2\} \rightarrow \mathbf{u}_{\text{ro}}\{3\}$ and for $\Omega = 0.1620$ rad s^{-1}. The reason behind this phenomenon is that, for $\Omega = 0.1620$ rad s^{-1}, the corresponding open-loop system exhibits a resonance at the frequency of 0.068 Hz, which is attributed to a flexible mode in the spinning spacecraft.

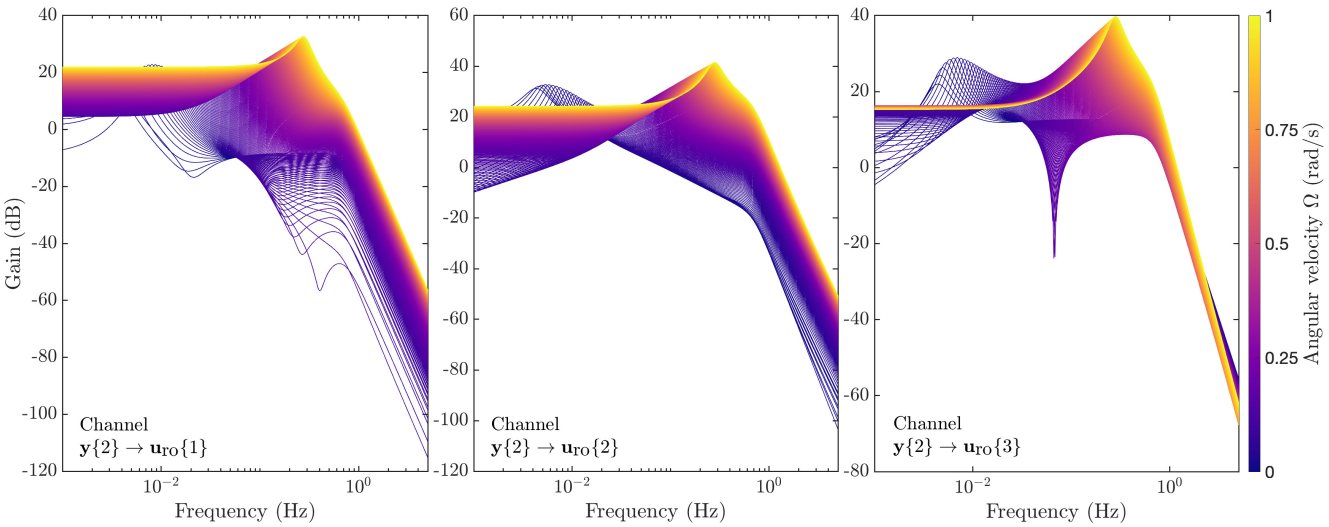

Fig. 6 Gains of $\mathbf{F}_{\text{ro}}(\text{s})\widehat{\mathbf{K}}_{\text{LPV}}(\text{s}, \Omega)$ for different values of the scheduling parameter $\Omega \in [0, 1]$ ($\mathbf{y}\{2\} \rightarrow \mathbf{u}_{\text{ro}}$ transfer functions).

This study is merely a glimpse of the potential offered by the TITOP multibody approach. Using this approach to build a model of any multibody flexible structure in LFR form enables the robust control design for a flexible system characterized by uncertainties and time-varying dynamics, all while meeting performance requirements.

5 Conclusion

This paper outlined a study on the modeling, analysis and control of a spinning spacecraft mission scenario, which is marked by complex and challenging interactions. To address this complexity, a linear fractional representation of the system was built, parameterized according to the angular velocity of the spacecraft. The paper also provides a valuable insight into the dynamics of the satellite, which includes

a central body, two flexible booms and two tip masses. This multibody modeling approach and analysis offers a practical understanding of the behavior of such systems under spinning conditions, which can be beneficial for the design and operation of similar missions, like THOR and Cluster. The paper also provides a detailed overview of the controller synthesis procedure, highlighting how to account for the different requirements and performance limits.

Appendix A: Change of frame

In order to assemble linear TITOP models between each other and/or to connect them to the main body, the Direct Cosine Matrix (DCM) $\mathbf{P}_{\mathcal{R}_a/\mathcal{R}_b}$ between the frame $\mathcal{R}_a$ attached to the body $\mathcal{A}$ and the frame $\mathcal{R}_b$ attached to the body $\mathcal{B}$ must be taken into account in the propagation of the wrench and motion vector variations. Let P be the point where $\mathcal{A}$ is connected to $\mathcal{B}$. Then, it follows that:

$$\begin{aligned}
\left[\delta\mathbf{W}_{\mathcal{A}/\mathcal{B},P}\right]_{\mathcal{R}_b} &= \underbrace{\operatorname{diag}\left(\mathbf{P}_{\mathcal{R}_a/\mathcal{R}_b}, \mathbf{P}_{\mathcal{R}_a/\mathcal{R}_b}\right)}_{\mathbf{P}^{\times 2}_{\mathcal{R}_a/\mathcal{R}_b}} \left[\delta\mathbf{W}_{\mathcal{A}/\mathcal{B},P}\right]_{\mathcal{R}_a} \\
\left[\delta\mathbf{m}^{\mathcal{B}}_{P}\right]_{\mathcal{R}_b} &= \underbrace{\operatorname{diag}\left(\mathbf{P}^{\times 2}_{\mathcal{R}_a/\mathcal{R}_b}, \mathbf{P}^{\times 2}_{\mathcal{R}_a/\mathcal{R}_b}, \mathbf{P}^{\times 2}_{\mathcal{R}_a/\mathcal{R}_b}\right)}_{\mathbf{P}^{\times 6}_{\mathcal{R}_a/\mathcal{R}_b}} \left[\delta\mathbf{m}^{\mathcal{A}}_{P}\right]_{\mathcal{R}_a}
\end{aligned} \tag{10}$$

Acknowledgments

This work was funded by ISAE-SUPAERO.

References

[1] A. D. Wright, C. E. Smith, R. W. Thresher, and J. L. C. Wang. Vibration Modes of Centrifugally Stiffened Beams. *Journal of Applied Mechanics*, 49(1):197–202, 03 1982. ISSN: 0021-8936. DOI: 10.1115/1.3161966.

[2] L. Puig, A. Barton, and N. Rando. A review on large deployable structures for astrophysics missions. *Acta Astronautica*, 67(1):12–26, 2010. ISSN: 0094-5765. DOI: https://doi.org/10.1016/j.actaastro.2010.02.021.

[3] C. P. Escoubet, M. Fehringer, and M. Goldstein. The cluster mission. *Annales Geophysicae*, 19(10/12):1197–1200, 2001. DOI: 10.5194/angeo-19-1197-2001.

[4] A. Vaivads, A. Retinò, J. Soucek, Yu. V. Khotyaintsev, F. Valentini, C. P. Escoubet, O. Alexandrova, M. André, S. D. Bale, M. Balikhin, and et al. Turbulence heating observer – satellite mission proposal. *Journal of Plasma Physics*, 82(5):905820501, 2016. DOI: 10.1017/S0022377816000775.

[5] Ahmed A. Shabana. Flexible multibody dynamics: Review of past and recent developments. *Multibody System Dynamics*, 1(2):189–222, 1997. DOI: 10.1023/a:1009773505418.

[6] Ricardo Rodrigues, Daniel Alazard, Francesco Sanfedino, Tommaso Mauriello, and Paolo Iannelli. Modeling and analysis of a flexible spinning euler-bernoulli beam with centrifugal stiffening and softening: A linear fractional representation approach with application to spinning spacecraft. 2024. DOI: 10.48550/ARXIV.2401.17519.

[7] Francesco Sanfedino, Daniel Alazard, Valérie Pommier-Budinger, Alexandre Falcoz, and Fabrice Boquet. Finite element based n-port model for preliminary design of multibody systems. *Journal of Sound and Vibration*, 415:128–146, 2018. ISSN: 0022-460X. DOI: https://doi.org/10.1016/j.jsv.2017.11.021.

[8] Daniel Alazard, J. Alvaro Perez, Christelle Cumer, and Thomas Loquen. Two-input two-output port model for mechanical systems. DOI: 10.2514/6.2015-1778.

[9] Hari Hara Sudhan Murali, Daniel Alazard, Luca Massotti, Finn Ankersen, and Chiara Toglia. Mechanical-attitude controller co-design of large flexible space structures. In Joël Bordeneuve-Guibé, Antoine Drouin, and Clément Roos, editors, *Advances in Aerospace Guidance, Navigation and Control*, pages 659–678, Cham, 2015. Springer International Publishing. ISBN: 978-3-319-17518-8.

[10] Jose Alvaro Perez, Daniel Alazard, Thomas Loquen, Christelle Cumer, and Christelle Pittet. Linear dynamic modeling of spacecraft with open-chain assembly of flexible bodies for ACS/structure co-design. In *Advances in Aerospace Guidance, Navigation and Control*, pages 639–658. Springer International Publishing, 2015. DOI: 10.1007/978-3-319-17518-8$_3$7.

[11] José Alvaro Perez Gonzalez, Daniel Alazard, Thomas Loquen, Christelle Pittet, and Christelle Cumer. Flexible multibody system linear modeling for control using component modes synthesis and double-port approach. *Journal of Dynamic Systems, Measurement, and Control*, 138(12):121004, December 2016. DOI: 10.1115/1.4034149.

[12] R. Rodrigues, V. Preda, F. Sanfedino, and D. Alazard. Modeling, robust control synthesis and worst-case analysis for an on-orbit servicing mission with large flexible spacecraft. *Aerospace Science and Technology*, 129:107865, 2022. ISSN: 1270-9638. DOI: https://doi.org/10.1016/j.ast.2022.107865.

[13] Daniel Alazard and Francesco Sanfedino. Satellite dynamics toolbox library (sdtlib) - user's guide, March 2021. `https://oatao.univ-toulouse.fr/28756/`.

[14] Ricardo Rodrigues, Francesco Sanfedino, Daniel Alazard, Valentin Preda, and Javier Olucha. Linear parameter-varying gain-scheduled attitude controller for an on-orbit servicing mission involving flexible large spacecraft and fuel sloshing. In *ESA GNC and ICATT Conference 2023*, Sopot, Poland, June 2023.

[15] Hidenori Murakami, Oscar Rios, and Thomas Joseph Impelluso. A theoretical and numerical study of the dzhanibekov and tennis racket phenomena. *Journal of Applied Mechanics*, 83(11), Sept. 2016. DOI: 10.1115/1.4034318.

[16] John F. Hall. Problems encountered from the use (or misuse) of rayleigh damping. *Earthquake Engineering & Structural Dynamics*, 35(5):525–545, 2006. DOI: https://doi.org/10.1002/eqe.541.

[17] Pierre Apkarian and Dominikus Noll. Nonsmooth $\mathcal{H}_\infty$ Synthesis. *IEEE Transactions on Automatic Control*, 51(1):71–86, 2006. DOI: 10.1109/TAC.2005.860290.

[18] Valentin Preda, Francesco Sanfedino, Samir Bennani, Fabrice Boquet, and Daniel Alazard. Robust and adaptable dynamic response reshaping of flexible structures. *Journal of Sound and Vibration*, 468:115086, 2020. ISSN: 0022-460X. DOI: https://doi.org/10.1016/j.jsv.2019.115086.

[19] Francesco Sanfedino, Valentin Preda, and Davide Oddenino. Integrated modeling of microvibrations induced by solar array drive mechanism for worst-case end-to-end analysis and robust disturbance estimation. *Mechanical Systems and Signal Processing*, 163:108168, 06 2021. DOI: 10.1016/j.ymssp.2021.108168.

[20] A Packard and J Doyle. The complex structured singular value. *Automatica*, 29(1):71–109, 1993. ISSN: 0005-1098. DOI: https://doi.org/10.1016/0005-1098(93)90175-S.